

Surface-Plasmon-Assisted Control of Ultrafast Optical Relaxation Traces

Maxim Andreevich Kiryanov, Ilya Alekseevich Novikov, Aleksandr Yurievich Frolov, Tatyana Viktorovna Dolgova, and Andrey Anatolyevich Fedyanin*

The time-dependent response of a material to a short laser pulse excitation directly reflects ultrafast physical processes within the material. In optical pump-probe experiments these processes can be observed due to laser-induced modification of material dielectric permittivity. In nanostructured systems resonant sensitivity of optical response to dielectric permittivity may provide a strong dependence of the relaxation trace on the probe wavelength. In this work, an anomalous wavelength-dependent temperature nonlinearity of the optical response of a plasmonic crystal on the picosecond timescale is shown, controlled by the system parameters and observed in the spectral vicinity of a surface plasmon resonance. A practical method for adjusting the picosecond relaxation traces of optical response is proposed on the basis of resonant probe. The effect is demonstrated experimentally and numerically. The phenomenological description is proposed.

1. Introduction

Small-scale light control is a rapidly growing application area for optical computing and communications. There are two broad areas of research — active nanophotonics and nanoplasmonics which are dealing with problems of real-time control of light beams. Over the past decades, significant progress has been made in creating reconfigurable optical resonant metaatoms and metasurfaces for subwavelength-scale light manipulation. A wide variety of approaches to reconfigure and switch plasmonic, all-dielectric and hybrid systems have been developed. The examples are electro-optical GHz plasmonic phase modulator,^[1] magneto-optical chiral-plasmonic modulator,^[2] thermal tuning of optical phase-change-material antennas,^[3] low-loss metasurfaces based on phase-change materials controlled by mid-IR nanosecond laser pulses^[4] or electric current,^[5] liquid crystal-based metasurfaces tunable with an electric^[6] or magnetic^[7] fields, plasmonic display based on catalytic metasurfaces,^[8] electrically controlled terahertz graphene metasurface,^[9] Goos–Hänchen-assisted

spatially-resolved magneto-optical intensity modulation,^[10] second harmonic generation in dichalcogenide monolayers boosted by high-Q metasurface,^[11] multimodal hybrid magnetoplasmonic metasurface for tunable magneto-optical Kerr effect enhancement,^[12] Poincaré sphere coverage with plasmonic crystals,^[13] reconfigurable photoinduced THz metasurface^[14] and others.

An all-optical switching approach provides possibilities for ultrafast wavefront control for beam shape, frequency conversion polarization and direction manipulation.^[15] Various designs and physical realizations were demonstrated including surface-plasmon waveguides^[16] and plasmonic 1D crystals,^[17] silicon-on-insulator ring resonator,^[18]

2D photonic microcavity,^[19] metal-insulator nanocavities with epsilon-near-zero modes,^[20] graphene-photonic crystal system supporting Bloch surface waves^[21] and graphene-plasmonic metasurface,^[22] semiconductor, and all-dielectric Mie-resonant,^[23,24] quasi-BIC^[25] and non-local^[26] metasurfaces.

A more difficult task of the active nanophotonics is to obtain desired picosecond time traces of optical response. The challenge arises in neuromorphic photonic computations,^[27,28] spiking neural networks,^[29] and dynamical memristors,^[30] which aim to mimic principals of a human brain. Biological synapses exhibit a variety of complex behaviors, such as spike timing-dependent plasticity,^[31] interaction between short-term and long-term memory,^[32] paired pulse facilitation,^[33] spike frequency adaptation.^[34] These phenomena are mathematically described using systems of coupled differential equations with nonlinear membrane conductance.^[35,36] Photonic implementations^[37–39] of these principals are based on fast initial excitation and subsequent two-exponential relaxation processes with a nonlinear relationship between excitatory postsynaptic current and presynaptic stimulation.

This kind of evolution can be expected from nanoplasmonic systems optical response.^[40–44] Femtosecond optical pump induces a substantially non-equilibrium energy distribution of electrons^[45] and subsequent bi-exponential relaxation.^[46] The characteristic times of these processes can be controlled by manipulating the shape and size of plasmonic particles.^[41] The potential of ultrafast active plasmonics has been demonstrated on the example of the active modulation of the phase, polarization,

M. A. Kiryanov, I. A. Novikov, A. Y. Frolov, T. V. Dolgova, A. A. Fedyanin
Faculty of Physics
Lomonosov Moscow State University
Moscow 119991, Russia
E-mail: fedyanin@nanolab.phys.msu.ru

 The ORCID identification number(s) for the author(s) of this article can be found under <https://doi.org/10.1002/lpor.202500053>

DOI: 10.1002/lpor.202500053

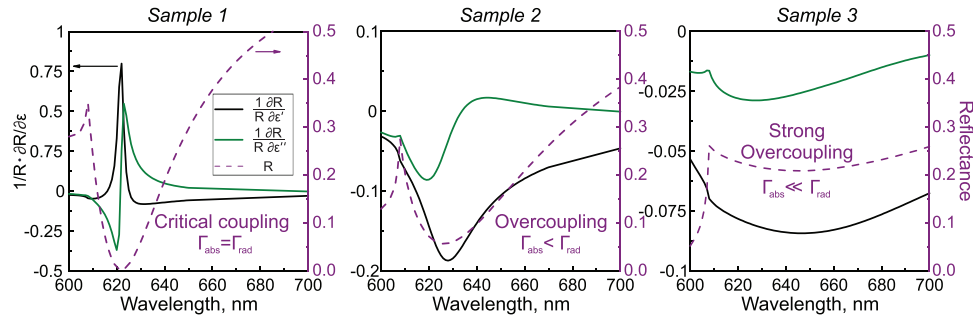


Figure 1. Calculated spectra of derivatives of reflectance by real (black curve) and imaginary (green curve) parts of dielectric permittivity, normalized to reflectance, along with simulated reflectance spectra (purple curve).

and amplitude of light through the nonlinear modification of the optical response of a plasmonic crystal that supports subradiant, high Q , and polarization-selective resonance modes.^[47] Nobel metal plasmonic particles can exhibit a wavelength-dependent transient optical response in the broad spectral region near the interband transition^[48] enabling a high on-off switching ratio.^[49] The anomalously strong changes to the ultrafast temporal and spectral response were observed in gold nanodisks caused by plasmon-induced electron injection.^[50] The ultrafast laser-induced dynamics of non-equilibrium electron spill-out in nanoplasmonic bilayers was used as a way to control surface plasmon dispersion.^[51] Inhomogeneous spacetime distribution of photogenerated hot carriers induces a transient symmetry breaking in a plasmonic metasurface. The process results in transient dichroism and paves the way for high-speed modulation of light polarization.^[52] 1D magnetoplasmonic crystal allows separation of ultrafast demagnetization and temperature dynamics.^[53,54] Anomalous relaxation process was observed at the polariton mode of hybrid metal-dielectric metasurface, while plasmon mode demonstrated typical for bulk gold dynamics.^[55] The electron population decays through electron-electron interactions, creating a hot electron distribution followed by relaxation via electron-phonon scattering, which is conventionally described by the two-temperature model (TTM):^[46,56,57]

$$\begin{cases} \gamma T_e \frac{dT_e}{dt} = k \nabla^2 T_e + G(T_p - T_e) + P(t, x, y, z) \\ C_p \frac{dT_p}{dt} = G(T_e - T_p) \end{cases} \quad (1)$$

where T_e, T_p are electron and phonon temperatures, G is electron-phonon coupling constant, $k = k_0 T_e / T_p$ is electron thermal conductivity, $\gamma T_e, C_p$ are electron and phonon heat capacities, $P(t, x, y, z)$ is the heat source. Sub-picosecond optical response of plasmonic systems follows electron and phonon temperatures dynamics,^[58] which, in turn, is defined by material constants and geometry.

In this paper, a practical approach to tailoring the picosecond relaxation traces of optical response is proposed on the basis of plasmonic crystals. Light-to-surface-plasmon coupling efficiency determines the sensitivity of surface plasmons to external stimuli and provides flexible control of the nonlinearity of reflectance on the picosecond timescale after excitation by a pump

pulse. The effect is most pronounced under critical coupling conditions.^[59,60] It is shown experimentally and numerically that the features allow the ultrafast temporal trace to be adjusted on demand by tuning the probe wavelength or angle of incidence.

2. Experimental Samples

A set of three 1D all-nickel plasmonic crystals with different surface corrugation depths was used. All samples had the same spatial period of 500 nm and surface shape close to a sinusoidal one. The corrugation depth values h were 90, 125, and 165 nm for Sample 1, Sample 2, and Sample 3, respectively. More details on sample fabrication and characterization are available in the Supporting Information. The samples support excitation of surface plasmons (SP), which are electromagnetic waves propagating along the metal-dielectric interface, arising from the resonant coupling of incident photons to free electron gas at the metal surface.^[61,62] The SP dispersion law is determined by dielectric permittivity of both constituent media, making SP optical response resonantly sensitive to the material properties at the boundary:

$$k_{sp}(\omega) = \frac{\omega}{c} \sqrt{\frac{\epsilon_d \epsilon_m}{\epsilon_d + \epsilon_m}} \quad (2)$$

where k_{sp} - SP wave-vector, ϵ_d and ϵ_m are dielectric permittivity of the two media. Since momentum mismatch between free-space photons and SP, surface plasmons require specific conditions to be excited by a plane wave. The diffraction grating enables the fulfillment of the phase-matching condition between the incident wave and the SP mode via the reciprocal lattice vector. In case of 1D grating, the condition takes the form:

$$k_0 \sin \theta = \text{Re}[k_{sp}] + 2\pi/d \quad (3)$$

where k_0 is the wavenumber of the incident light, θ is the angle of incidence, and d is the grating period. A comprehensive analysis of the resonant optical properties in the visible spectral range of the samples can be found elsewhere.^[63]

The main feature of the set is different light-to-surface plasmon coupling regimes, previously studied experimentally and numerically. Both steady-state reflectance spectra measurements and calculations (**Figure 1**, purple curves) revealed the corrugation depth h influence on the radiation losses Γ_{rad} , allowing

fulfillment of the light-to-SP critical coupling condition: equality of radiative and absorption losses, $\Gamma_{rad} = \Gamma_{abs}$.^[59,60] The latter is provided by the Sample 1 with the most profound SP resonance in the reflectance spectrum along with the highest field localization at the nickel-air interface. The other two samples demonstrate over-coupling regime. Sample 3 was the least effective in terms of plasmonic excitation. A more thorough analysis of the corrugation depth influence on light-to-SP coupling and the reflectance spectra of plasmonic crystals can be found in the manuscript.^[63]

3. Spectra Control

Let us consider sensitivity of plasmonic crystal optical response to material properties perturbation as a derivative of reflectance R by real and imaginary parts of dielectric permittivity, $\epsilon = \epsilon' + i\epsilon''$, normalized to R (Figure 1).

Derivatives were obtained from numerical simulations by the formulas:

$$\begin{aligned} \frac{\partial R}{\partial \epsilon'} &= \frac{R(\epsilon'_0 + d\epsilon', \epsilon''_0) - R(\epsilon'_0, \epsilon''_0)}{d\epsilon'} \\ \frac{\partial R}{\partial \epsilon''} &= \frac{R(\epsilon'_0, \epsilon''_0 + d\epsilon'') - R(\epsilon'_0, \epsilon''_0)}{d\epsilon''} \end{aligned} \quad (4)$$

where $R(\epsilon'_0, \epsilon''_0)$ is calculated reflectance of a plasmonic crystal with nickel dielectric permittivity from,^[64] and $R(\epsilon'_0 + d\epsilon', \epsilon''_0)$, $R(\epsilon'_0, \epsilon''_0 + d\epsilon'')$ are reflectance with a small perturbation of the dielectric permittivity $d\epsilon^{(i)} \ll \epsilon^{(i)}$. The Sample 1 with critical coupling demonstrates the sharpest spectral feature and the greatest sensitivity to dielectric permittivity. For this sample the spectral dependence of $1/R \cdot \partial R/\partial \epsilon'$ has symmetric peak and $1/R \cdot \partial R/\partial \epsilon''$ lineshape appears as antisymmetric curve. The increase of a corrugation depth reduces sensitivity of SP-resonant reflectance to dielectric permittivity, especially to the imaginary part, and yields more symmetrical spectral features.

The spectral lineshapes of reflectance and their dependencies on h may be explained as follows. Perturbation of dielectric permittivity induces modification of complex SP wave-vector. Differentiation of SP dispersion law $k_{sp}(\omega)$ (Equation (2)) by real and imaginary parts at nickel dielectric permittivity values $\epsilon_{Ni}(\lambda = 620 \text{ nm})$ ^[64] leads to:

$$\frac{\partial k_{sp}}{\partial \epsilon'} = \frac{\omega}{c} (-4 + 12i) 10^{-3}, \quad \frac{\partial k_{sp}}{\partial \epsilon''} = \frac{\omega}{c} (-12 - 4i) 10^{-3} \quad (5)$$

Change of ϵ' dominantly modifies the imaginary part of wave-vector, which corresponds to plasmon absorption losses Γ_{abs} , and, therefore, alters resonance width and light-to-SP coupling efficiency, that results in symmetric peak in $1/R \cdot \partial R/\partial \epsilon'$ spectrum for all samples. Sample 1 demonstrates the highest values of $1/R \cdot \partial R/\partial \epsilon'$ because of near-zero reflectance at the center of resonance, $\partial R/\partial \epsilon'$ values are commensurate for all three samples. In turn, change of ϵ'' mostly affects $Re[k_{sp}]$ and induces a shift of the SP resonance. Since Sample 1 provides the narrowest and most profound resonant lineshape, impact of SP shift to $1/R \cdot \partial R/\partial \epsilon''$ is the greatest (within the studied set) and manifests itself as asymmetric spectral feature. Influence of the SP shift on

reflectance for the other two samples is significantly weaker, so they demonstrate lower both $1/R \cdot \partial R/\partial \epsilon''$ and $\partial R/\partial \epsilon''$ values.

Any active plasmonic effect spectrum may be described by superposition of green and black curves in Figure 1. For example, in the case of heating, measured value is differential reflectance:

$$\frac{\Delta R}{R} = \frac{R_{pump} - R_0}{R_0} \quad (6)$$

where R_{pump} is the reflectance of the heated sample, R_0 is the initial reflectance. The increase of temperature alters sample dielectric permittivity providing modification of reflectance. Differential reflectance spectrum can be expressed as:

$$\begin{aligned} \frac{\Delta R}{R}(\lambda) &= \int \frac{1}{R} \frac{\partial R}{\partial \epsilon'}(\lambda) d\epsilon' + \int \frac{1}{R} \frac{\partial R}{\partial \epsilon''}(\lambda) d\epsilon'' \\ &= \left[\frac{1}{R} \frac{\partial R}{\partial \epsilon'}(\lambda) \right] \int \left(\frac{\partial \epsilon'}{\partial T} \right) dT + \left[\frac{1}{R} \frac{\partial R}{\partial \epsilon''}(\lambda) \right] \int \left(\frac{\partial \epsilon''}{\partial T} \right) dT \end{aligned} \quad (7)$$

where terms in square brackets correspond to plasmonic properties defined by plasmonic crystal geometry and provide dominant impact to spectral features, while terms in round brackets are defined by material condensed-matter-properties and are the same for all samples. Integral values are defined by thermodynamic properties and heating process and can be considered as weights.

The same formalism can be applied to angular spectra: according to Equation (3), both the wavelength of incident light and angle of incidence determine the SP phase-matching condition in a similar way. The angular spectrum is an analogue of the wavelength spectrum in the case of grating coupling.^[61]

4. Experimental Results

The ultrafast measurements were carried out in the pump-probe scheme. Regeneratively amplified Ti:sapphire laser with 50-fs pulse duration, 800-nm central wavelength, and 1 kHz repetition rate was used as a source of radiation. The pump pulse of 7 mJ/cm² fluence was normally incident on the sample surface and was far from SP resonance. All pump-induced changes were probed by the broad (550–750 nm) TM-polarized supercontinuum pulse. The angle of incidence of the probe pulse was 12°. Detailed description of experimental setup can be found in the [supporting information](#).

The differential reflectance $\Delta R/R(\lambda, \tau)$ spectra were measured for all three samples. $R_{pump} = R(\lambda, \tau)$ in Equation (6) is the reflectance of the pumped sample at the τ pump-probe time delay and λ is a probe wavelength, $R_0 = R_0(\lambda)$ is unpumped sample reflectance.

The obtained $\Delta R/R(\lambda, \tau)$ data are shown in Figure 2 (top panels) as 2D heat maps. One can see that corrugation depth affects both spectral lineshape and absolute values of $\Delta R/R(\lambda, \tau)$. As a reference sample, bulk nickel plate (grating with zero corrugation depth) was used.

The reflectance spectra $R_0(\lambda)$ (purple curves in Figure 2, bottom panels) indicates the SP excitation for all three samples with the central wavelength of 625, 635, and 675 nm, respectively.

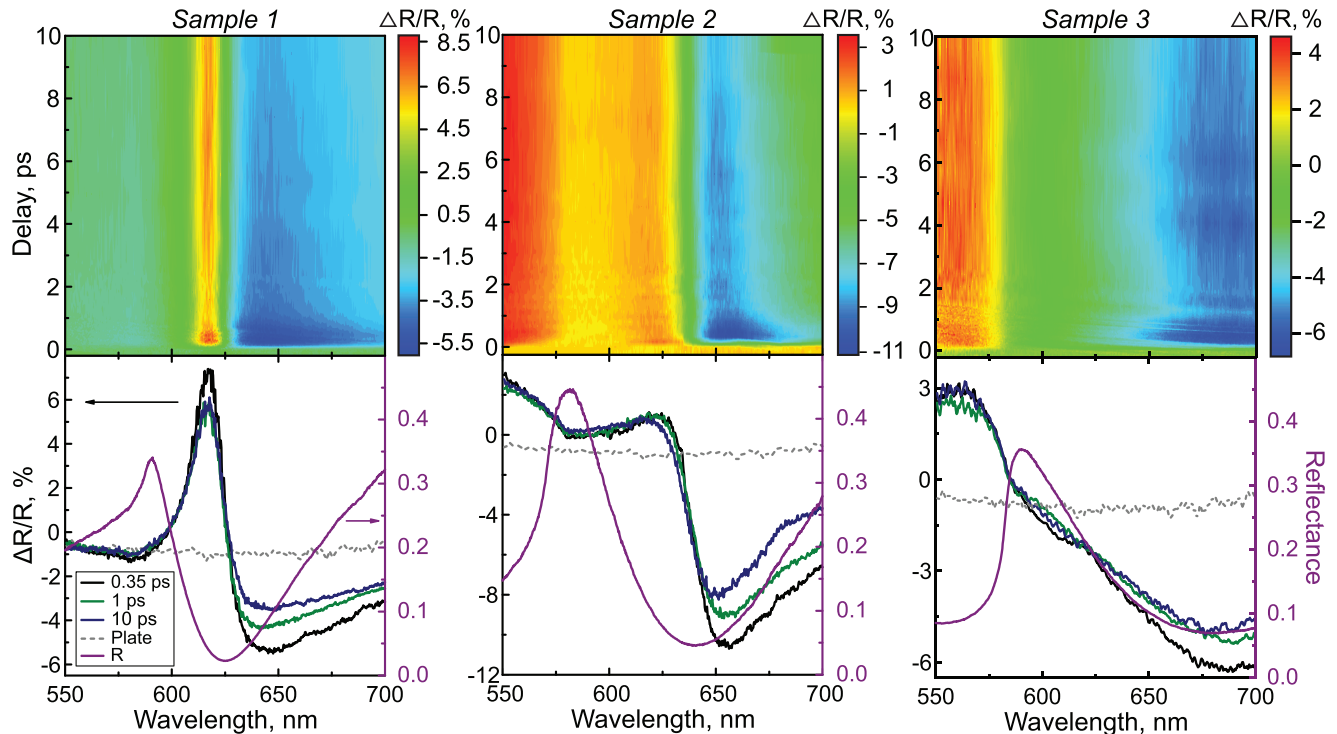


Figure 2. Top panels: 2D heat maps representing the differential reflectance dependence on wavelength λ and pump-probe delay τ for three samples. Bottom panels: differential reflectance spectra $\Delta R/R(\lambda)$ at various pump-probe delays τ (black, green, and blue curves) along with the reflectance (purple curve) for the set of studied samples and reference nickel plate (grey dashed curve).

The peaks in the reflectance spectra correspond to the Rayleigh anomaly arising from the propagation of the -1^{st} diffraction order along the sample surface. The red-edge dips refer to the Wood anomaly associated with SP excitation. The angular dependence of these spectral features, confirming their nature, was demonstrated previously.^[63] Heating of the sample surface by the pump pulse induces modification of real and imaginary parts of dielectric permittivity resulting in shift, broadening or amplitude variation of the SP resonance, as described in Section 3, and provides modification of the reflectance spectra $R_0(\lambda)$. The most significant changes in $\Delta R/R(\lambda)$ spectrum for all time delays appear at the vicinity of SP resonance (black, green and blue curves in Figure 2, bottom panels). The SP-resonant $\Delta R/R(\lambda)$ lineshape for Sample 1 is asymmetrical curve with two extrema and a sign change. Such lineshape is the result of resonance shifting upon heating. The differential reflectance spectrum at the vicinity of SP for Sample 3 represents the symmetrical curve with only one extremum and is attributed to the heat-induced reduction of the resonance amplitude. Sample 2 represents an intermediate case. $\Delta R/R(\lambda)$ lineshapes can be qualitatively described by the superposition of black and green curves on Figure 1 with different signs. Broadening of experimental spectra compared to the calculated ones is caused by finite angular width of probe pulse about $^\circ$.

Sample 2 and Sample 3 reflectance spectra demonstrate additional dip at the blue edge of studied range. It corresponds to the peak in differential reflectance spectra. This is so called standing wave surface plasmon,^[63,65] that emerged on the walls of grating grooves. This resonance is beyond the scope of the paper, more details can be found in ref. [63].

The $\Delta R/R$ evolutions (Figure 3) agrees with the results of previous studies in nickel^[46,66,67] and other metals.^[68] and reflects laser-induced carrier dynamics.

The latter is governed by the interaction of laser radiation with two subsystems of metal: free electrons and phonons of lattice. In turn, modification of reflectance is associated with dependence of dielectric permittivity on both electron and phonon temperatures. The initial differential reflectance growth is attributed to the excitation of electrons to the energy above the Fermi level through the pulse energy absorption and energy transfer to the neighboring cold electrons through electron–electron collisions known as electron thermalization. Typical value of electron thermalization time, τ_{ee} , in nickel is tens of femtoseconds.^[69] The process is essentially non-steady-state, thus neither the temperature, nor the distribution function can be assigned. The temporal resolution of our setup is insufficient to extract the exact τ_{ee} value. The $\Delta R/R(\tau)$ reaches the extrema at 250 fs that is consistent with the previous works with similar setup parameters. As soon as the thermalization process is over, one can say that the electron subsystem is in the state of equilibrium and the electron temperature T_e can be introduced. Thermalized electrons are described by broad Fermi distribution at a temperature T_e .^[46]

The growth of $\Delta R/R(\tau)$ is followed by an exponential decay with a time constant τ_{ep} referring to the electron–phonon relaxation, the process of energy transfer from hot electrons to phonons of the lattice. The process lasts for several picoseconds in nickel^[66,69,70] until the thermal equilibrium between the electrons and phonons is achieved. The subsequent relaxation is attributed to heat dissipation through phonon–phonon

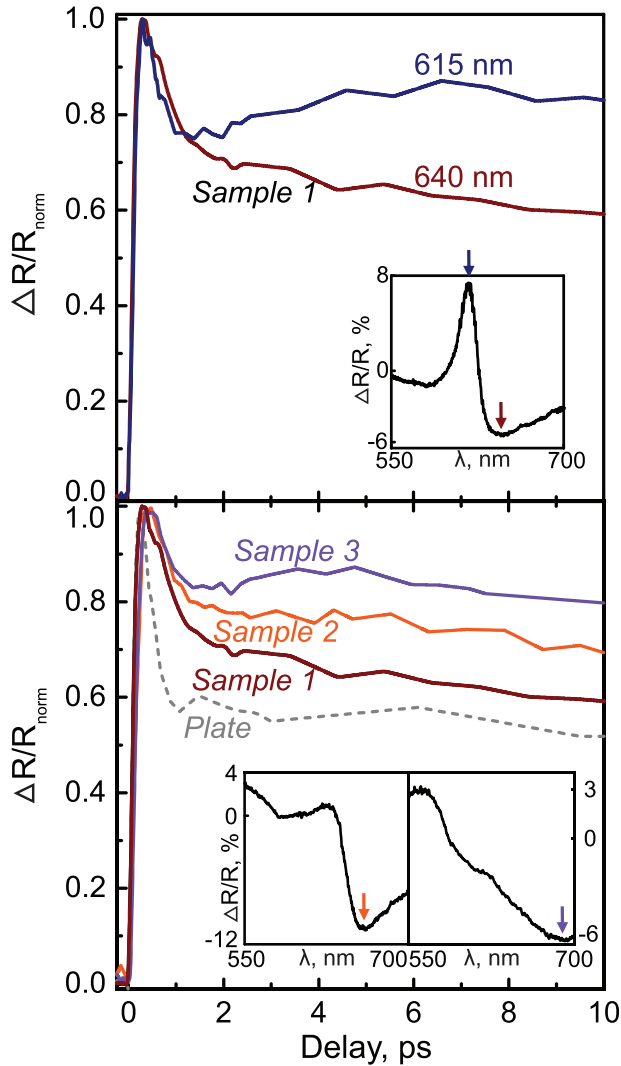


Figure 3. Normalized to maximum differential reflectance temporal dependencies $\Delta R/R(\tau)$ for the set of studied samples and reference nickel plate; arrows on the insets indicate spectral position of taken traces.

collisions with the typical duration of hundreds of picoseconds that is beyond the scope of consideration.

Curves in Figure 3 are taken at the wavelengths of the $\Delta R/R$ spectral dips. For nickel reference plate differential reflectance traces are almost spectrally independent. However, in contrast to the reference plate, sample's $\Delta R/R(\tau)$ trace vary with the wavelength and can qualitatively deviate from conventional traces for metals. The significant difference from bulk nickel dynamics is observed for Sample 1 at the vicinity of $\Delta R/R$ maximum (Figure 3, top panel). It is seen that instead of exponential decay, as in the reference sample, the differential reflectance dynamics at the blue edge of SP resonance shows an additional peak that lasts for several picoseconds. Still the dynamics at the red edge of SP resonance represents monotonous relaxation typical for nickel. Spectral dependence of differential reflectance evolution is observed also for the other two samples, but the relaxation curve change with probe wavelength is the most profound for Sample 1 with critical coupling and is the faintest for Sample 3.

Similar temporal features were observed in the case of ultrafast heating and probing of intraband transitions in gold plasmonic nanoparticles. A tunable transient optical response was demonstrated in Au nanomushrooms by combining intra- and interband pumping.^[49] Ultrafast heating of gold plasmonic particles beyond perturbative regime results in non-monotonic pump-probe relaxation traces, and the transient lineshape dependence on the probe wavelength.^[48] These effects are based on the material resonance in gold, whereas nickel exhibits no pronounced resonances in the optical spectrum. Therefore, the observed features in nickel plasmonic crystals can be associated solely with configurational resonances.

5. Temporal Trace Control

Let us first consider differential reflectance dynamics by simple mathematical approach in terms of TTM and reflectance sensitivity to dielectric permittivity. The evolution of optical response is defined by derivative dR/dt . For simplicity, the nickel skin layer is assumed to be homogeneously heated to some electron T_{eff}^e and phonon T_{eff}^p effective temperatures. Thus, the multiplier $\partial \epsilon^{(n)}/\partial T \cdot dT$ in Equation (7) can be transformed into $\partial \epsilon^{(n)}/\partial T_{eff}^e \cdot dT_{eff}^e + \partial \epsilon^{(n)}/\partial T_{eff}^p \cdot dT_{eff}^p$. Differentiation of Equation (7) by time leads to the expression:

$$\begin{aligned} \frac{d}{dt} \left(\frac{\Delta R}{R} \right) &= \frac{1}{R} \frac{\partial R}{\partial \epsilon'}(\lambda) \left(\frac{\partial \epsilon'}{\partial T_{eff}^e} \frac{dT_{eff}^e}{dt} + \frac{\partial \epsilon'}{\partial T_{eff}^p} \frac{dT_{eff}^p}{dt} \right) \\ &+ \frac{1}{R} \frac{\partial R}{\partial \epsilon''}(\lambda) \left(\frac{\partial \epsilon''}{\partial T_{eff}^e} \frac{dT_{eff}^e}{dt} + \frac{\partial \epsilon''}{\partial T_{eff}^p} \frac{dT_{eff}^p}{dt} \right) \end{aligned} \quad (8)$$

The studied anomalous temporal phenomenon occurs within the electron–phonon relaxation process during the first few picoseconds. Laser irradiation is over by this time, and heat flux is negligible, because hot electron diffusion takes place on a timescale of hundreds of femtoseconds and heat dissipation into bulk metal should be considered on hundreds of picosecond timescale.^[46,57] These assumptions allows deduction from TTM the following relation between electron and phonon temperature:

$$\gamma T_{eff}^e \frac{dT_{eff}^e}{dt} = -C_p \frac{dT_{eff}^p}{dt} \quad (9)$$

Inserting this expression into Eq. (8), one can obtain:

$$\begin{aligned} \frac{d}{dt} \left(\frac{\Delta R}{R} \right) &= \left[\frac{1}{R} \frac{\partial R}{\partial \epsilon'}(\lambda) \left(-\frac{C_p}{\gamma T_e} \frac{\partial \epsilon'}{\partial T_{eff}^e} + \frac{\partial \epsilon'}{\partial T_{eff}^p} \right) \right. \\ &+ \left. \frac{1}{R} \frac{\partial R}{\partial \epsilon''}(\lambda) \left(-\frac{C_p}{\gamma T_e} \frac{\partial \epsilon''}{\partial T_{eff}^e} + \frac{\partial \epsilon''}{\partial T_{eff}^p} \right) \right] \frac{dT_{eff}^p}{dt} \end{aligned} \quad (10)$$

Thus, there are three different contributions to the differential reflectance dynamics: the sensitivity of plasmonic optical response to dielectric permittivity, $1/R \cdot \partial R/\partial \epsilon$, the dependence of dielectric permittivity on temperature, $\partial \epsilon/\partial T_{eff}$, and the dynamics of phonon temperature, dT_{eff}^p/dt . The first term reflects the plasmonic properties of the system, the second term is determined

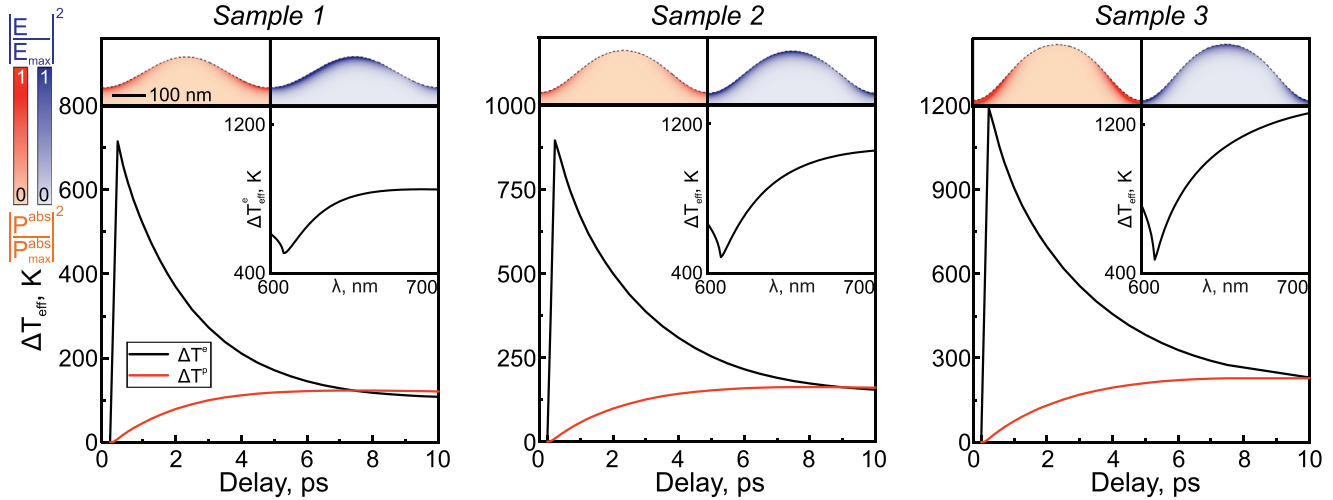


Figure 4. Top panels: spatial distribution of pump absorbed power (orange) and squared electric probe field (green), values are normalized by common maximal values. Bottom panels: Effective temperature (Equation (13)) temporal dependence for SP-resonant wavelengths; insets: effective electron temperature spectra at 250 fs time delay.

by the optical properties of the material and the third term relates to the thermodynamics. Since plasmonic term may drastically change over wavelengths, it allows one to vary the contribution of real and imaginary parts of dielectric permittivity dynamics to the overall differential reflectance evolution and tune the temporal trace by probe wavelength.

On the studied timescale phonon temperature monotonically rises, thus, to reproduce dynamics observed in the experiment (Figure 3), the term in square brackets in Equation (10) has to be both time and spectrally dependent. Temporal dependence is provided by the terms in round brackets. Meanwhile, the entire dynamics is governed by the plasmonic terms $1/R \cdot \partial R / \partial \epsilon$ acting as weights in the superposition. Depending on the wavelength they can either preserve the sign of the expression (on the timescale of τ_{ep}) or change it.

The temporal dependence of the round brackets (Equation (10)) is defined by dielectric permittivity dependencies on T_{eff}^e and T_{eff}^p . Since the heat capacity of an electron gas is linear with temperature, the thermal energy of electrons turns out to be quadratic with temperature, while the thermal energy of phonons is linear. It is known that in the case of Drude metals, the dielectric permittivity under heating changes due to modification of the electron collisions rate.^[58] Moreover, it depends linearly on the T^p ,^[58,71] and quadratically on the T^e ,^[72] but in both cases this dependence is linear with the pumped energy. However, substitution of $\epsilon(T_{eff}^e, T_{eff}^p) = aT_{eff}^e{}^2 + bT_{eff}^p$ into Equation (10) leads to time-independence of the multipliers in round brackets. Therefore, nonlinear dependence of dielectric permittivity on pump fluence should be considered. Since spectral discrepancy of $\Delta R/R(\tau)$ traces occurs at the delays far from initial hot electron peak, it seems more reasonable to choose the following dielectric permittivity dependence on temperature:

$$\epsilon^{(l)}(T_{eff}^e, T_{eff}^p) = a^{(l)} T_{eff}^e{}^2 + b^{(l)} T_{eff}^p + c^{(l)} T_{eff}^p{}^2 \quad (11)$$

where $a', a'', b', b'', c', c''$ are constants. Nonlinear temperature dependence of dielectric permittivity was experimentally ob-

served in nickel in steady-state experiments.^[73] Inserting dependence Equation (11) into Equation (10), one can obtain:

$$\frac{d}{dt} \left(\frac{\Delta R}{R} \right) = \left[\frac{1}{R} \frac{\partial R}{\partial \epsilon'}(\lambda) \left(-\frac{2a' C_p}{\gamma} + b' + 2c' T_{eff}^p \right) + \frac{1}{R} \frac{\partial R}{\partial \epsilon''}(\lambda) \left(-\frac{2a'' C_p}{\gamma} + b'' + 2c'' T_{eff}^p \right) \right] \frac{dT_{eff}^p}{dt} \quad (12)$$

To test the hypothesis, we carried out optical and temperature simulations. The simulated structures were designed to fully reproduce the configuration of the studied samples (period, surface shape and corrugation depth), as well as the conditions of the experiment (angle of incidence, polarization and pump fluence). First, electromagnetic simulations for pump and probe pulses were performed (top panels, Figure 4).

The spatial distribution of pump absorbed power corresponds to heating of the plasmonic crystals and defines spatial profile of the heat source $P(t, x, y)$ in TTM calculations. Note that off-resonant absorbance increases with corrugation depth. Temporal envelope of $P(t, x, y)$ was defined as 50 fs-width Gaussian. As a result of the TTM calculations, the spatio-temporal distributions of electron and phonon temperatures $T^{e(p)}(x, y, t)$ were obtained.

Since the temperature distribution as well as the probe pulse localization are inhomogeneous, no specific temperature value can be attributed to probed reflectance. Thus, effective probed temperatures $T_{eff}^{e(p)}(t, \lambda_{probe})$ (Figure 4) were introduced:

$$T_{eff}^{e(p)}(t, \lambda_{probe}) = \frac{\int_V |E(x, y, \lambda_{probe})|^2 T^{e(p)}(x, y, t) dV}{\int_V |E(x, y, \lambda_{probe})|^2 dV} \quad (13)$$

where $E(x, y, \lambda_{probe})$ is the probe electric field inside the plasmonic crystal and V is the plasmonic crystal volume. $T_{eff}^{e(p)}(t)$ should be considered as the effective temperatures, detected by the probe pulse. $T_{eff}^{e(p)}(t, \lambda_{probe})$ (Figure 4, insets) is lower at the center of

SP resonance and increases with wavelength (the blue edge is affected by the Rayleigh anomaly). The effective temperature is spectrally dependent because of different overlapping of the probe electric field and spatial temperature distributions, which depends on the probe wavelength. At the center of SP resonance, the electric field is localized along the plasmonic crystal surface resulting in the mismatch of the probe electric field and heated regions, while the off-resonant field is localized at plasmonic crystal grooves and overlaps with hot areas.

Increasing off-resonant absorption with corrugation depth leads to a higher maximal effective temperature (Figure 4). It explains the divergence between dR/R values (Figure 2, bottom panels) and SP sensitivity for the Samples 3 compared to the Sample 1 (Figure 1). Apart from different maximal effective temperatures of the samples, temperature dynamics is also different. The equilibrium between T_e and T_p is reached faster in gratings with smaller height. The slowdown is caused by heat diffusion along the plasmonic crystal walls.

To take into account inhomogeneous heating, derivatives of reflectance by dielectric permittivity were adjusted (Figure 5, insets).

Instead of homogeneous perturbation $\varepsilon = \varepsilon_0 + d\varepsilon$ in Equation (4), the spatial distribution of temperature was taken into account:

$$\tilde{\varepsilon}_{e(p)}^{(n)}(x, y, t) = \varepsilon_0^{(n)} + d\varepsilon \frac{T^{e(p)}(x, y, t) - T_0}{T_{eff}^{(p)}(t) - T_0} \quad (14)$$

where $d\varepsilon \ll \varepsilon$, T_0 is initial temperature, 293 K. Sample reflectance spectra were recalculated, and adjusted derivatives for electron and phonon temperatures were obtained (Figure 5, inset) using the following equation:

$$\frac{\partial \widetilde{R}}{\partial \varepsilon_{e(p)}'} = \frac{R(\tilde{\varepsilon}_{e(p)}'(x, y, t), \varepsilon_0') - R(\varepsilon_0', \varepsilon_0'')}{d\varepsilon} \quad (15)$$

The derivatives slightly depend on time due to heat diffusion. In contrast to the Figure 1, where black and green curves have different amplitudes for each sample, the corresponding curves in Figure 5 have comparable amplitudes, but spectrally separated extrema. The sample with the critical coupling provides maximal contrast between $1/R \cdot \partial \widetilde{R} / \partial \varepsilon'$ and $1/R \cdot \partial \widetilde{R} / \partial \varepsilon''$.

The temperature dynamics and adjusted derivatives were used to fit the experimental $\Delta R/R(\lambda, \tau)$ traces (Figure 5). The time integral of Equation (8) was used as the fitting function:

$$\frac{\Delta R}{R}(\tau, \lambda) = \alpha(\tau, \lambda) \Delta(T_{eff}^e)^2(\tau, \lambda) + \beta(\tau, \lambda) \Delta(T_{eff}^p)^2(\tau, \lambda) + \gamma(\tau, \lambda) \Delta T_{eff}^p(\tau, \lambda) \quad (16)$$

where functions $\alpha(\tau, \lambda)$, $\beta(\tau, \lambda)$, $\gamma(\tau, \lambda)$ were defined by the adjusted derivatives:

$$\begin{aligned} \alpha(\tau, \lambda) &= a' \frac{1}{R} \frac{\partial \widetilde{R}}{\partial \varepsilon_e'}(\tau, \lambda) + a'' \frac{1}{R} \frac{\partial \widetilde{R}}{\partial \varepsilon_e''}(\tau, \lambda) \\ \beta[\gamma](\tau, \lambda) &= b[c]' \frac{1}{R} \frac{\partial \widetilde{R}}{\partial \varepsilon_p'}(\tau, \lambda) + b[c]'' \frac{1}{R} \frac{\partial \widetilde{R}}{\partial \varepsilon_p''}(\tau, \lambda) \\ \gamma(\tau, \lambda) &= c' \frac{1}{R} \frac{\partial \widetilde{R}}{\partial \varepsilon_p'}(\tau, \lambda) + c'' \frac{1}{R} \frac{\partial \widetilde{R}}{\partial \varepsilon_p''}(\tau, \lambda) \end{aligned} \quad (17)$$

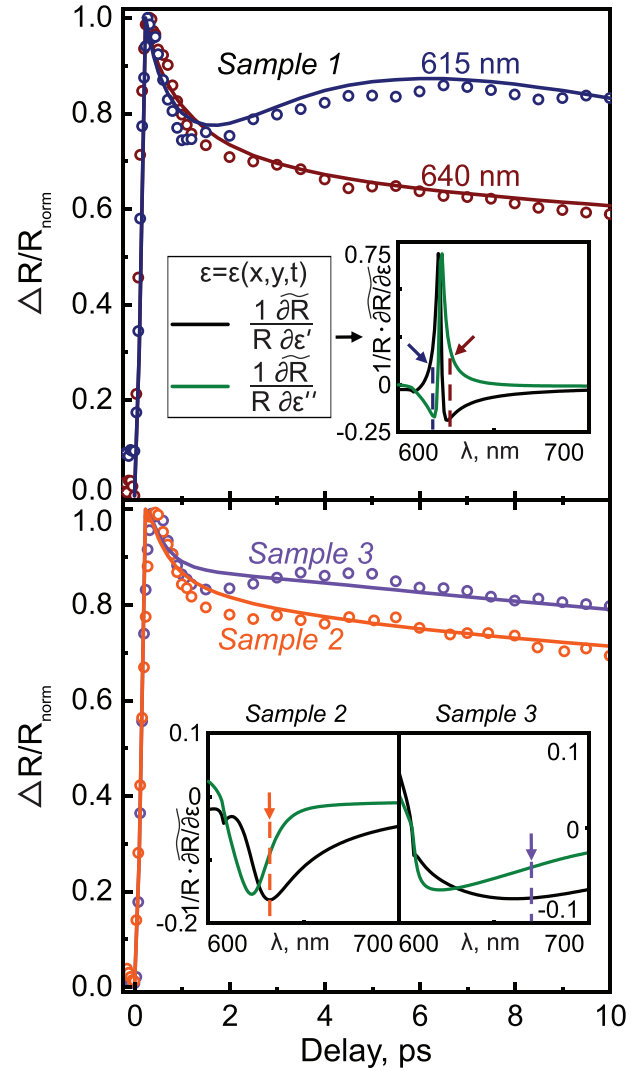


Figure 5. Calculated and experimental normalized differential reflectance temporal dependence; insets: calculated spectra of adjusted (Equation (15)) derivatives of reflectance by real (black curve) and imaginary (green curve) parts of dielectric permittivity, normalized to reflectance, arrows indicate wavelengths used in calculations.

and $a', a'', b', b'', c', c''$ were constants. TTM parameters g, γ, k, C_p as well as constants $a', a'', b', b'', c', c''$ were the same for all three samples and optimized to fit the experimental data. Probe wavelengths were also optimized for each experimental trace and turn out to coincide with the extrema of adjusted derivatives (arrows on insets of Figure 5). Fitting procedure was conducted simultaneously for three samples. TTM parameters, that provide the correct convergence of the calculated and the experimental data are: $g = 27 \times 10^{16} \text{ Wm}^{-3} \text{ K}^{-1}$, $\gamma = 1670 \text{ Jm}^{-3} \text{ K}^{-1}$, $k_0 = 99.3 \text{ Wm}^{-1} \text{ K}^{-1}$, $C_p = 3.26 \times 10^6 \text{ Jm}^{-1} \text{ K}^{-1}$. The values are consistent with previous experimental results.^[46,66,67,69,74]

Although the quadratic dependence of the dielectric constant on the phonon temperature was taken into account for all three samples, it showed up only in a narrow spectral window for the sample 1. The regions of resonant sensitivity of reflectance to real and imaginary parts of dielectric permittivity are spectrally sepa-

rated due to the critical coupling. In contrast, relation of ϵ' and ϵ'' contributions to the reflectance is spectrally uniform for the other two samples (Figure 5, insets).

The observed phenomena hold potential for neuromorphic computing applications. Photonic synapses, essential components in optical spiking neural networks, determine input weights for optical neurons. To replicate human brain plasticity, these devices must exhibit a transient optical response to spikes. Adaptive artificial synapses employ various bi-exponential decay processes to mimic short- and long-term memory. Electron-phonon and phonon-phonon relaxation processes can play this role on the picosecond timescale. In turn, the plasmonic-based synapse provides configurable transient response, adjustment of the relative levels of short- and long-term contributions and switching between potentiation and depression by changing operating wavelength. Nonlinear device functionalities become critical for implementing more complex synaptic features like paired-pulse facilitation, when preceding spikes influence neural responses to the subsequent spike. The demonstrated controllable effective temperature nonlinearity opens up the possibility to tune paired-pulse facilitation regime, otherwise defined by the material.

6. Conclusion

In conclusion, we have shown that the picosecond trace of optical relaxation can vary drastically for a nickel plasmonic crystal supporting the critical coupling regime. In a narrow spectral range the trace is non-monotonous and differs from the typical exponential decay. The effective nonlinearity of reflectance with respect to temperature becomes strongly wavelength-dependent, leading to qualitative differences between temporal traces for various probe spectral intervals. This effect enables tuning the temporal optical response of the plasmonic crystal and provides desired input power nonlinearity. Since SP resonant frequency is determined by both the angle of incidence and wavelength, the control can also be implemented by varying the probe angle. The studied effect can advance the development of all-optical picosecond-time-based reconfigurable neuromorphic synapse. Tuning capabilities of temporal traces and nonlinearity with input power allow adjustment of the short-term to long-term memory transition and tailoring of the paired-pulse facilitation.

Supporting Information

Supporting Information is available from the Wiley Online Library or from the author.

Acknowledgements

Authors thank Dr. V.V. Popov for samples fabrications. M.A. Kiryanov acknowledged the Foundation for the Advancement of Theoretical Physics and Mathematics BASIS for the scholarship award. Equipment provided by the MSU development programme (No. 0259-44-2022) was used in the experiment. This work was financially supported by Russian Science Foundation, project No. 24-12-00210.

Conflict of Interest

The authors declare no conflict of interest.

Data Availability Statement

The data that support the findings of this study are available from the corresponding author upon reasonable request.

Keywords

carrier dynamics, electron-phonon relaxation, nickel, plasmonic crystals, pump-probe spectroscopy, surface plasmons, ultrafast optics

Received: January 8, 2025

Revised: April 1, 2025

Published online:

- [1] A. Melikyan, L. Alloatti, A. Muslija, D. Hillerkuss, P. C. Schindler, J. Li, R. Palmer, D. Korn, S. Muehlbrandt, D. Van Thourhout, B. Chen, R. Dinu, M. Sommer, C. Koos, M. Kohl, F. W., L. J., *Nat. Photon.* **2014**, *8*, 229.
- [2] I. Zubritskaya, N. Maccaferri, X. Inchausti Ezeiza, P. Vavassori, A. Dmitriev, *Nano Lett.* **2018**, *18*, 302.
- [3] M. A. Kats, R. Blanchard, P. Genevet, Z. Yang, M. M. Qazilbash, D. Basov, S. Ramanathan, F. Capasso, *Opt. Lett.* **2013**, *38*, 368.
- [4] A. Leitis, A. Heßler, S. Wahl, M. Wuttig, T. Taubner, A. Tittl, H. Altug, *Adv. Funct. Mater.* **2020**, *30*, 1910259.
- [5] S. Abdollahramezani, O. Hemmatyar, M. Taghinejad, H. Taghinejad, A. Krasnok, A. A. Eftekhar, C. Teichrib, S. Deshmukh, M. A. El-Sayed, E. Pop, M. Wuttig, A. Alù, W. Cai, A. Adibi, *Nat. Commun.* **2022**, *13*, 1696.
- [6] M. Decker, C. Kremers, A. M., I. Staude, A. E. Miroshnichenko, D. Chigrin, D. N. Neshev, C. Jagadish, Y. S. Kivshar, *Opt. Express* **2013**, *21*, 8879.
- [7] Y. V. Izdebskaya, Z. Yang, V. G. Shvedov, D. N. Neshev, I. V. Shadrivov, *Nano Lett.* **2023**, *23*, 9825.
- [8] X. Duan, S. Kamin, N. Liu, *Nat. Commun.* **2017**, *8*, 14606.
- [9] L. Ju, B. Geng, J. Horng, C. Girit, M. Martin, Z. Hao, H. A. Bechtel, X. Liang, A. Zettl, Y. R. Shen, F. Wang, *Nat. Nanotechnol.* **2011**, *6*, 630.
- [10] A. V. Makarova, A. A. Nerovnyaya, D. N. Gulkin, V. V. Popov, A. Y. Frolov, A. A. Fedyanin, *ACS Photonics* **2024**, *11*, 1619.
- [11] A. A. Nazarenko, A. M. Chernyak, A. I. Musorin, A. S. Shorokhov, L. Ding, V. Valuckas, M. Nonahal, I. Aharonovich, S. T. Ha, A. I. Kuznetsov, A. A. Fedyanin, *Nanophotonics* **2024**, *13*, 3429.
- [12] A. I. Musorin, A. V. Chetvertukhin, T. V. Dolgova, H. Uchida, M. Inoue, B. S. Luk'Yanchuk, A. A. Fedyanin, *Appl. Phys. Lett.* **2019**, *115*, 151102.
- [13] M. Shcherbakov, M. Dobynde, T. Dolgova, D.-P. Tsai, A. Fedyanin, *Phys. Rev. B* **2010**, *82*, 193402.
- [14] I. A. Novikov, M. A. Kiryanov, V. Stadnichuk, T. V. Dolgova, A. A. Fedyanin, *JETP Lett.* **2024**, *119*, 665.
- [15] M. Maiuri, A. Schirato, G. Cerullo, G. Della Valle, *ACS Photonics* **2024**, *11*, 2888.
- [16] K. F. MacDonald, Z. L. Sámson, M. I. Stockman, N. I. Zheludev, *Nat. Photon.* **2009**, *3*, 55.
- [17] M. R. Shcherbakov, P. P. Vabishchevich, V. V. Komarova, T. V. Dolgova, V. I. Panov, V. V. Moshchalkov, A. A. Fedyanin, *Phys. Rev. Lett.* **2012**, *108*, 253903.
- [18] V. R. Almeida, C. A. Barrios, R. R. Panepucci, M. Lipson, *Nature* **2004**, *431*, 1081.
- [19] X. Hu, P. Jiang, C. Ding, H. Yang, Q. Gong, *Nat. Photon.* **2008**, *2*, 185.
- [20] J. Kuttruff, D. Garoli, J. Allerbeck, R. Krahn, A. De Luca, D. Brida, V. Caligiuri, N. Maccaferri, *Commun. Phys.* **2020**, *3*, 114.
- [21] A. A. Popkova, A. A. Chezhegov, M. G. Rybin, I. V. Soboleva, E. D. Obraztsova, V. O. Bessonov, A. A. Fedyanin, *Adv. Opt. Mater.* **2022**, *10*, 2101937.

- [22] L. Xu, J. He, W. Tang, C. Yang, L. Han, L. Zhang, H. Zhu, S. Liu, C. Liu, M. Qiu, G. Li, X. Chen, *Laser Photonics Rev.* **2024**, *18*, 2300643.
- [23] M. R. Shcherbakov, P. P. Vabishchevich, A. S. Shorokhov, K. E. Chong, D.-Y. Choi, I. Staudé, A. E. Miroshnichenko, D. N. Neshev, A. A. Fedyanin, Y. S. Kivshar, *Nano Lett.* **2015**, *15*, 6985.
- [24] M. R. Shcherbakov, S. Liu, V. V. Zubyuk, A. Vaskin, P. P. Vabishchevich, G. Keeler, T. Pertsch, T. V. Dolgova, I. Staudé, I. Brener, A. A. Fedyanin, *Nat. Commun.* **2017**, *8*, 1.
- [25] Z. Yang, M. Liu, D. Smirnova, A. Komar, M. R. Shcherbakov, T. Pertsch, D. N. Neshev, *Nanophotonics* **2024**, *13*, 2173.
- [26] G. Crotti, M. Akturk, A. Schirato, V. Vinel, A. A. Trifonov, I. C. Buchvarov, D. N. Neshev, R. Proietti Zaccaria, P. Laporta, A. Lemaître, G. Leo, G. Cerullo, M. Maiuri, G. Della Valle, *Light Sci. Appl.* **2024**, *13*, 204.
- [27] B. J. Shastri, A. N. Tait, T. Ferreira de Lima, W. H. P. Pernice, H. Bhaskaran, C. D. Wright, P. R. Prucnal, *Nat. Photon.* **2021**, *15*, 102.
- [28] D. Ivanov, A. Chezhegov, D. Larionov, *Front. Neurosci.* **2022**, *16*, 959626.
- [29] K. Yamazaki, V.-K. Vo-Ho, D. Bulsara, N. Le, *Brain Sci.* **2022**, *12*, 863.
- [30] S. Kumar, X. Wang, J. P. Strachan, Y. Yang, W. D. Lu, *Nat. Rev. Mater.* **2022**, *7*, 575.
- [31] N. Caporale, Y. Dan, *Annu. Rev. Neurosci.* **2008**, *31*, 25.
- [32] D. Norris, *Psychol. Bull.* **2017**, *143*, 992.
- [33] S. L. Jackman, W. G. Regehr, *Neuron* **2017**, *94*, 447.
- [34] G. E. Ha, E. Cheong, *Exp. Neurobiol.* **2017**, *26*, 179.
- [35] E. M. Izhikevich, *IEEE Trans. Neural Netw. Learn. Syst.* **2004**, *15*, 1063.
- [36] R. Brette, W. Gerstner, *J. Neurophysiol.* **2005**, *94*, 3637.
- [37] I. S. Balashov, A. A. Chezhegov, A. S. Chizhov, A. A. Grunin, K. V. Anokhin, A. A. Fedyanin, *Opto-Electron. Sci.* **2023**, *2*, 230016.
- [38] G. K. Gupta, I.-J. Kim, Y. Park, M.-K. Kim, J.-S. Lee, *ACS Appl. Mater. Interfaces* **2023**, *15*, 18055.
- [39] J.-Y. Chen, D.-L. Yang, F.-C. Jhuang, Y.-H. Fang, J.-S. Benas, F.-C. Liang, C.-C. Kuo, *Adv. Funct. Mater.* **2021**, *31*, 2105911.
- [40] A. N. Koya, M. Romanelli, J. Kuttruff, N. Henriksson, A. Stefancu, G. Grinblat, A. De Andres, F. Schnur, M. Vanzan, M. Marsili, M. Rahaman, A. Viejo Rodríguez, T. Tapani, H. Lin, B. D. Dana, J. Lin, G. Barbillon, R. Proietti Zaccaria, D. Brida, D. Jariwala, L. Veisz, E. Cortés, S. Corni, D. Garoli, N. Maccaferri, *Appl. Phys. Rev.* **2023**, *10*, 021318.
- [41] L. V. Besteiro, P. Yu, Z. Wang, A. W. Holleitner, G. V. Hartland, G. P. Wiederrecht, A. O. Govorov, *Nano Today* **2019**, *27*, 120.
- [42] A. Muravitskaya, A. Movsesyan, O. Avalos-Ovando, V. A. Bahamondes Lorca, M. A. Correa-Duarte, L. V. Besteiro, T. Liedl, P. Yu, Z. Wang, G. Markovich, A. O. Govorov, *ACS Photonics* **2023**, *11*, 68.
- [43] M. Taghinejad, W. Cai, *ACS Photonics* **2019**, *6*, 1082.
- [44] L. Agiotis, M. Meunier, *Laser Photonics Rev.* **2022**, *16*, 2200076.
- [45] P. O'Keeffe, D. Catone, L. Di Mario, F. Toschi, M. Magnozzi, F. Bisio, A. Alabastri, R. Proietti Zaccaria, A. Toma, G. Della Valle, A. Paladini, *Laser Photonics Rev.* **2021**, *15*, 2100017.
- [46] S.-S. Wellershoff, J. Hohlfeld, J. Gädde, E. Matthias, *Appl. Phys. A* **1999**, *69*, S99.
- [47] M. Taghinejad, H. Taghinejad, Z. Xu, K.-T. Lee, S. P. Rodrigues, J. Yan, A. Adibi, T. Lian, W. Cai, *Nano Lett.* **2018**, *18*, 5544.
- [48] A. Schirato, G. Crotti, M. Gonçalves Silva, D. C. Teles-Ferreira, C. Manzoni, R. Proietti Zaccaria, P. Laporta, A. M. de Paula, G. Cerullo, G. Della Valle, *Nano Lett.* **2022**, *22*, 2748.
- [49] X. Dong, Y. He, R. Gao, K. Yang, J. Wang, W. Yang, J. Li, B. Ren, M.-D. Li, Z. Yang, *Nano Lett.* **2025**, *25*, 4005.
- [50] H. Harutyunyan, A. B. Martinson, D. Rosenmann, L. K. Khorashad, L. V. Besteiro, A. O. Govorov, G. P. Wiederrecht, *Nat. Nanotechnol.* **2015**, *10*, 770.
- [51] A. Avdizhiyan, W. Janus, M. Szpytma, T. Ślęzak, M. Przybylski, M. Chrobak, V. Roddatis, A. Stupakiewicz, I. Rzdolski, *Nano Lett.* **2024**, *24*, 466.
- [52] A. Schirato, M. Maiuri, A. Toma, S. Fugattini, R. Proietti Zaccaria, P. Laporta, P. Nordlander, G. Cerullo, A. Alabastri, G. Della Valle, *Nat. Photon.* **2020**, *14*, 723.
- [53] I. A. Novikov, M. A. Kiryanov, P. K. Nurgalieva, A. Y. Frolov, V. V. Popov, T. V. Dolgova, A. A. Fedyanin, *Nano Lett.* **2020**, *20*, 8615.
- [54] I. A. Novikov, M. A. Kiryanov, A. Y. Frolov, V. V. Popov, T. V. Dolgova, A. A. Fedyanin, *JETP Lett.* **2023**, *118*, 574.
- [55] M. A. Kiryanov, G. S. Ostanin, T. V. Dolgova, M. Inoue, A. A. Fedyanin, *JETP Lett.* **2023**, *117*, 196.
- [56] S. I. Anisimov, B. L. Kapeliovich, T. L. Perel'Man, *J. Exp. Theor. Phys.* **1974**, *39*, 375.
- [57] A. Block, M. Liebel, R. Yu, M. Spector, Y. Sivan, F. García de Abajo, N. F. van Hulst, *Sci. Adv.* **2019**, *5*, eaav8965.
- [58] T. Stoll, P. Maioli, A. Crut, N. Del Fatti, F. Vallée, *Eur. Phys. J. B* **2014**, *87*, 1.
- [59] Y. Ra'di, A. Krasnok, A. Alú, Virtual critical coupling, *ACS Photonics* **2020**, *7*, 1468.
- [60] A. Yariv, *IEEE Photonics Technol. Lett.* **2002**, *14*, 483.
- [61] H. Raether, *Springer-Verlag, Berlin, Germany* **1988**.
- [62] W. L. Barnes, A. Dereux, T. W. Ebbesen, *Nature* **2003**, *424*, 824.
- [63] M. A. Kiryanov, A. Y. Frolov, I. A. Novikov, P. A. Kipp, P. K. Nurgalieva, V. V. Popov, A. A. Ezhov, T. V. Dolgova, A. A. Fedyanin, *APL Photonics* **2022**, *7*, 026104.
- [64] P. Johnson, R. Christy, *Phys. Rev. B* **1974**, *9*, 5056.
- [65] M. Sobnack, W. Tan, N. Wanstall, T. Preist, J. Sambles, *Phys. Rev. Lett.* **1998**, *80*, 5667.
- [66] E. Beaupaire, J.-C. Merle, A. Daunois, J.-Y. Bigot, *Phys. Rev. Lett.* **1996**, *76*, 4250.
- [67] J. Hohlfeld, S.-S. Wellershoff, J. Gädde, U. Conrad, V. Jähnke, E. Matthias, *Chem. Phys.* **2000**, *251*, 237.
- [68] C.-K. Sun, F. Vallée, L. Acioli, E. Ippen, J. Fujimoto, *Phys. Rev. B* **1993**, *48*, 12365.
- [69] M. van Kampen, J. T. Kohlhepp, W. de Jonge, B. Koopmans, R. Coehoorn, *J. Phys. Condens. Matter* **2005**, *17*, 6823.
- [70] J. Hohlfeld, E. Matthias, R. Knorren, K. H. Bennemann, *Phys. Rev. Lett.* **1997**, *78*, 4861.
- [71] J. B. Smith, H. Ehrenreich, *Phys. Rev. B* **1982**, *25*, 923.
- [72] G. Parkins, W. Lawrence, R. Christy, *Phys. Rev. B* **1981**, *23*, 6408.
- [73] S. Zollner, T. N. Nunley, D. P. Trujillo, L. G. Pineda, L. S. Abdallah, *Appl. Surf. Sci.* **2017**, *421*, 913.
- [74] Z. Lin, L. V. Zhigilev, V. Celli, *Phys. Rev. B* **2008**, *77*, 075133.